

Incorporation of the Rotor-Equivalent Wind Speed into the Weather Research and Forecasting Model's Wind Farm Parameterization

STEPHANIE REDFERN

*Department of Atmospheric and Oceanic Sciences, and the Cooperative Institute for Research in Environmental Sciences,
University of Colorado Boulder, Boulder, Colorado*

JOSEPH B. OLSON

*Global Systems Division, National Oceanic and Atmospheric Administration, and Cooperative Institute for
Research in Environmental Sciences, University of Colorado Boulder, Boulder, Colorado*

JULIE K. LUNDQUIST

*Department of Atmospheric and Oceanic Sciences, University of Colorado Boulder, Boulder, and
National Renewable Energy Laboratory, Golden, Colorado*

CHRISTOPHER T. M. CLACK

Vibrant Clean Energy, Boulder, Colorado

(Manuscript received 30 May 2018, in final form 18 January 2019)

ABSTRACT


Wind power installations have been increasing in recent years. Because wind turbines can influence local wind speeds, temperatures, and surface fluxes, weather forecasting models should consider their effects. Wind farm parameterizations do currently exist for numerical weather prediction models. They generally consider two turbine impacts: elevated drag in the region of the wind turbine rotor disk and increased turbulent kinetic energy production. The wind farm parameterization available in the Weather Research and Forecasting (WRF) Model calculates this drag and TKE as a function of hub-height wind speed. However, recent work has suggested that integrating momentum over the entire rotor disk [via a rotor-equivalent wind speed (REWS)] is more appropriate, especially for cases with high wind shear. In this study, we implement the REWS in the WRF wind farm parameterization and evaluate its impacts in an idealized environment, with varying amounts of wind speed shear and wind directional veer. Specifically, we evaluate three separate cases: neutral stability with low wind shear, high stability with high wind shear, and high stability with nonlinear wind shear. For most situations, use of the REWS with the wind farm parameterization has marginal impacts on model forecasts. However, for scenarios with highly nonlinear wind shear, the REWS can significantly affect results.

1. Introduction

Wind energy has become increasingly important over recent years. Wind energy contributed 6.3% of electric power to the United States in 2017 (U.S. Energy Information Administration 2018) and as of the fourth quarter (4Q) 2017, the United States has 87 077 MW of

cumulative, installed wind power capacity, with 28 668 MW under construction (AWEA Data Services 2017). Globally, 539.6 GW of wind power capacity is installed, with 52.6 GW of new construction added in 2017 (Global Wind Energy Council 2018). Wind power will likely continue to expand as the economics of renewable energy are becoming progressively favorable (Williams et al. 2017; AWEA Data Services 2017). With this growth in mind, operational weather forecasting models may need to consider how turbines affect the atmosphere.

Observational studies have demonstrated that wind farms can have microscale effects on atmospheric

 Denotes content that is immediately available upon publication as open access.

Corresponding author: Stephanie Redfern, stephanie.redfern@colorado.edu

properties such as winds, temperature, and heat and moisture fluxes. Wind farms extract kinetic energy from the wind, resulting in wakes (Lissaman 1979; Högström et al. 1988; Wang and Prinn 2010; Iungo et al. 2013; Smith et al. 2013). Several studies have found a nighttime warming trend downwind of wind farms (Baidya Roy and Traiteur 2010; Zhou et al. 2012; Smith et al. 2013; Rajewski et al. 2013; Armstrong et al. 2016; Rajewski et al. 2016), which is likely due to vertical mixing induced by turbine operation. Daytime increases in upward latent heat flux and downward CO₂ flux also occur (Rajewski et al. 2013). As these effects are not negligible, they should be considered in weather models.

To account for turbine impacts, wind farm parameterizations (WFPs) have been developed for mesoscale models (Baidya Roy et al. 2004; Baidya Roy 2011; Fitch et al. 2012). Baidya Roy et al. (2004) implemented a parameterization in the Regional Atmospheric Modeling System (RAMS) to evaluate how wind farms impact local-scale atmospheric dynamics. This WFP modeled turbines as both a momentum sink and a turbulence source, and showed that turbines have small impacts on surface sensible heat fluxes and evapotranspiration, presumably due to the increased near-ground turbulence. The study also found that turbines significantly reduce wind speeds around hub height. Blahak et al. (2010) and Fitch et al. (2012) later developed WFPs for the Weather Research and Forecasting (WRF) Model. Fitch et al. (2012) expanded upon Blahak et al.'s (2010) parameterization efforts by basing the momentum extracted from the atmosphere on the manufacturer-specified turbine thrust coefficient.

Some studies have compared WRF wind farm modeling results with observations, and most note some bias in the parameterization. Comparisons between the WRF WFP and power data taken at the Horns Rev wind farm off the coast of Denmark found that simulations with the WFP qualitatively reproduced wake structures but overall underforecasted power production for downstream turbines (Jimenez et al. 2015). An additional study comparing WRF WFP mesoscale simulations with data collected in an onshore wind farm in the U.S. Midwest came to a similar conclusion: the WFP improved wind power predictions, but again underestimated power production at downwind turbines (Lee and Lundquist 2017a). Conversely, Vanderwende et al. (2016) compared the WRF WFP to turbine-resolving large-eddy simulations and found in this case that the WFP overestimated TKE production and underestimated the magnitudes of the wakes. And, regarding impacts on near-surface temperatures, Xia et al. (2017) showed that although the WFP reproduced larger-scale, wind farm-driven warming signals consistent with observations, it

also caused a nighttime, downwind cooling effect that is currently unverified by measurements.

Before including a WFP in an operational weather forecasting model, the WFP should accurately represent the interactions of wind turbines with atmospheric events, for all possible scenarios. Aside from the suspected bias in the WRF WFP, certain situations may arise in which it does not behave as expected. For example, during mountain–valley cold pool mix-out events, strongly stratified cold air is trapped and shielded from higher wind speeds aloft. Robust vertical wind shear develops at the interface between the cold pool and free troposphere, producing turbulence, which begins to erode the stable layer. Eventually, the overhead winds descend low enough to intersect the turbine rotor layer, resulting in episodes of very high wind shear profiles across the rotor plane. These cold pool events in complex topography occur with regularity; 120 events occurred in the Columbia River basin between 1989 and 1999 (Whiteman et al. 2001), and in the recent second Wind Forecasting Improvement Project (WFIP2), at least 8 have been recognized between November 2015 and December 2016 (Wilczak et al. 2018, manuscript submitted to *Bull. Amer. Meteor. Soc.*). Because the WRF WFP only considers hub-height wind speeds in its physics calculations, it may return inaccurate results for cold pool mix-outs.

In light of this potential for error and aforementioned biases in the WRF WFP, we propose two modifications that aim to improve the representation of wind farms in high wind shear environments. In the following section, we summarize the existing WRF WFP and discuss the components of a revised WRF WFP (RWFP). The RWFP testing setup is explained in sections 3 and 4, testing results are presented in section 5, and section 6 details the conclusions from this study.

2. Wind farm parameterization

WRF is a popular community modeling framework (Skamarock et al. 2008; Powers et al. 2017) upon which many regional weather models have been built, including the National Oceanic and Atmospheric Administration (NOAA)'s High Resolution Rapid Refresh (HRRR). Included in the WRF distribution is a wind farm parameterization, which has been well documented (Fitch et al. 2012, 2013a; Fitch 2015, 2016) and has been employed at regional (Jimenez et al. 2015; Volker et al. 2015; Lee and Lundquist 2017a,b) and continental scales (Vautard et al. 2014).

a. Current distribution of WFP

The Fitch et al. (2012, hereafter F2012) parameterization comes packaged in the WRF distribution. Users

must specify turbine properties, such as hub-height, rotor diameter, maximum power output, and they must also provide power and thrust coefficient curves. Most of the parameterization derivations are explained in detail in F2012 and Fitch et al. (2013b). Updates made to the WFP in 2015 are documented in the model code and addressed in a note (Fitch 2016). Some important aspects and assumptions of the current WRF WFP are highlighted below.

1) POWER GENERATION

Power generation in the model assumes that turbines are driven by the hub-height wind speeds, with a constant sea level air density of $\rho_a = 1.23 \text{ kg m}^{-3}$. It should be noted that this assumption may introduce calculation errors at high elevations. However, for the code to account for variable atmospheric pressure would also require one to obtain pressure-specific power curves for each turbine used in a simulation, as the power curve delivered with the turbine is rated based on empirical testing done at sea level. Often this information is proprietary, so the WFP as it is assumes sea level air density throughout the domain. Power production from an individual grid cell is defined as

$$P_{ij} = \frac{1}{2} (C_p \rho_a |\mathbf{U}_H|^3 A_T N_T)_{ij}. \quad (1)$$

Here, $|\mathbf{U}_H|$ is hub-height wind speed, C_p is the turbine power coefficient at the hub-height wind speed, A_T is the turbine swept area defined as $A_T = (\pi/4)D^2$, and N_T is the number of turbines per grid cell, located at (i, j) . Power output is calculated every time step for each grid cell containing a turbine.

2) TKE AND MOMENTUM TENDENCIES

The WRF WFP assumes that all turbines in a particular grid cell are driven by the mean wind speed in that grid cell and subgrid-scale heterogeneity is ignored. Further, the momentum drag and turbulent kinetic energy (TKE) (or kinetic energy per unit mass in $\text{m}^2 \text{s}^{-2}$) produced by each turbine are evenly distributed through the cell and no explicit wake interactions occur between turbines in a given model grid cell. To calculate the sum of individual turbines F2012 introduced a *wind farm density* variable, which is defined as the number of turbines per square meter. The wind farm density is multiplied through the drag and TKE tendency equations to determine the full impact of the turbines on a per-grid-cell basis.

The parameterization assumes that the drag force induced by the turbines on the atmosphere is defined by the basic drag equation:

$$F_D = \frac{1}{2} \rho_a \mathbf{U}^2 A_T C_D. \quad (2)$$

Here, \mathbf{U} is the velocity vector, defined as $\mathbf{U} = (u, v)$, and C_D is the coefficient of drag—in this case, it is equivalent to the turbine thrust coefficient C_T , which is a function of wind velocity and is specific to the turbine used.

The change in atmospheric kinetic energy (KE) (in $\text{kg m}^2 \text{s}^{-2}$) from air–turbine interactions, therefore, can be derived as follows:

$$\frac{\partial \text{KE}_{\text{Drag}}}{\partial t} = -\frac{1}{2} \int_{A_T} C_T \rho_a |\mathbf{U}|^3 dA. \quad (3)$$

For numerical simulations, this equation must be discretized across model vertical levels, wind components, and horizontal grid cells, and must account for the possibility of multiple turbines per grid cell. Additionally, the assumption is made that turbines do not affect vertical winds. In the WRF WFP, Eq. (3) is therefore discretized as

$$\frac{\partial \text{KE}_{ijk}}{\partial t} = \frac{\partial |\mathbf{U}|_{ijk}}{\partial t} |\mathbf{U}|_{ijk} \rho_a (z_{k+1} - z_k) \Delta x \Delta y, \quad (4)$$

where i and j represent model grid locations in the horizontal and k represents individual model vertical layers. The wind vector in Eq. (4), therefore, is taken from the grid cell under evaluation (not necessarily at hub height). By defining the wind farm density variable as N_t , the momentum tendency can be then derived as

$$\frac{\partial |\mathbf{U}|_{ijk}}{\partial t} = -\frac{1}{2} \frac{N_t^{ij} C_T |\mathbf{U}|_{ijk}^2 A_{ijk}}{(z_{k+1} - z_k)}. \quad (5)$$

The parameterization assumes that all energy extracted by turbines that is not converted to electricity instead generates TKE:

$$\frac{\partial \text{TKE}_{ijk}}{\partial t} = \frac{1}{2} \frac{N_t^{ij} C_{\text{TKE}} |\mathbf{U}|_{ijk}^3 A_{ijk}}{(z_{k+1} - z_k)}, \quad (6)$$

with the TKE coefficient $C_{\text{TKE}} = C_p - C_T$.

Revisions to the WRF code since F2012 have added in a “normalization” factor (Blahak et al. 2010) that is multiplied through Eqs. (5) and (6) for each WFP-active grid cell. As shown in Eq. (1), the estimate of power using the turbine-specific power curve is only a function of the hub-height wind speed. However, as shown in Eqs. (5) and (6), the multilayer total tendency calculations employed in the WFP are summations that use wind speeds valid at each model level. The normalization factor aims to make these estimates equivalent, allowing changes in the model wind and TKE to be consistent with total wind energy production, thus conserving energy. This factor is defined as follows:

$$ec = \frac{\frac{1}{2}(C_p \rho_a |\mathbf{U}_H|^3 A_T N_T)_{ij}}{\sum_{k=\text{turbine bottom}}^{\text{turbine top}} \frac{1}{2}(C_p \rho_a |\mathbf{U}_{ijk}|^3 A_{ijk} N_T)_{ijk}}. \quad (7)$$

The normalization factor and the power equation are the only two calculations that use hub-height wind speed. It follows that, similarly, the rotor-equivalent wind speed, derived in the following two sections, will only affect these two equations.

b. Rotor-equivalent wind speed

In the equations above, the hub-height wind speed dictates how each turbine responds to the atmosphere. However, the assumption that hub-height wind speed and direction are representative of all wind flow across the rotor plane is not always substantiated. Several studies address this issue. [Wagner et al. \(2009\)](#) demonstrates that the use of wind speeds at hub height to represent the entire wind profile across the rotor swept area has led to errors in power forecasting. Although using hub-height wind speeds for power production may be an adequate approximation for small turbines, as turbines grow in size the uncertainties introduced by this assumption also grow.

The rotor-equivalent wind speed (REWS) addresses this problem by integrating momentum across the rotor disk. By dividing the swept area into a series of horizontal segments, one can calculate a weighted average of the wind speeds:

$$REWS = \sum_{k=1}^N \frac{A_{ijk}}{A_T} |\mathbf{U}_{ijk}|. \quad (8)$$

Here, A_k is the cross-sectional swept area within a model layer being evaluated, A_T is the total cross-sectional swept area of the turbine blades, and $|\mathbf{U}_k|$ is the magnitude of the velocity vector in the layer being evaluated.

c. REWS, considering veer

Just as wind speed may vary across the turbine rotor disk, wind direction may also vary. We therefore also examine the implications of wind directional shear across the rotor swept plane, or as we specifically define it in this paper to include both clockwise and counter-clockwise shear, veer. Veer can reduce the projected turbine power output (compared with the assumption that all wind intersecting the turbine is aligned normal to the rotor plane). Additionally, veer can influence the TKE generation and energy extracted from the atmosphere in the same manner.

[Choukulkar et al. \(2016\)](#) and [Clack et al. \(2016\)](#) define this veer component in their formulations of equivalent

wind speed. This definition builds upon the previously defined REWS by adding directionality into the equation, as follows:

$$REWS_d = \sum_{k=1}^N \frac{A_{ijk}}{A_T} |\mathbf{U}_{ijk}| \cos(\theta_{ijk}). \quad (9)$$

Here, θ_k is the angle between the wind direction and the turbine axis, defined as the direction the turbine is facing. This value is zero at hub height. All other variables are as previously defined. In the RWFP, we replace the hub-height wind speed $|\mathbf{U}_H|$ in Eq. (1) with $REWS_d$ defined in Eq. (9). To account for veer in KE loss and TKE generation, a factor of $\cos(\theta_{ijk})$ is multiplied through Eqs. (5) and (6).

Model layer depth can vary dynamically during a simulation due to changing air temperatures. This should not significantly affect the RWFP calculation, as the parameterization is relatively insensitive to vertical resolution ([Fitch et al. 2012](#)) and changes on the order of doubling or halving the resolution are needed to effect 5%–10% changes in wake structures. Even with up to 10°C temperature changes, layer depth would only see a 3% change, which is not large enough to meaningfully affect wakes.

3. Modeling approach

All simulations are conducted using the Advanced Research version of the WRF Model (WRF-ARW) ([Skamarock et al. 2008](#)), version 3.8.1, with NOAA internal edits to the code ([Benjamin et al. 2016](#)). The idealized test environment has been simplified: the land surface, radiation, cumulus, and microphysics schemes have all been turned off, as in [F2012](#).

a. Domain setup

The test environment attempts to replicate the idealized setup used in [F2012](#). Two domains are set up in a nested configuration, each with 202×202 horizontal grid cells. The fine domain has a horizontal resolution of 1 km and is centered in the coarse domain, which has a horizontal resolution of 3 km. The coarse grid has open radiative boundary conditions. The lateral boundary conditions of the fine grid are horizontally interpolated from the coarse grid at each time step. The domains are coupled using a one-way interaction, where values from the interior domain are not returned to and cannot influence the outer domain. The time step is 9 s for the coarse grid and 3 s for the fine grid. There are 81 vertical levels, with the model top set at 20 km. A total of 28 vertical layers fall within the lower 200 m of the model and 11 layers intersect the rotor swept area ([Fig. 1](#)). The

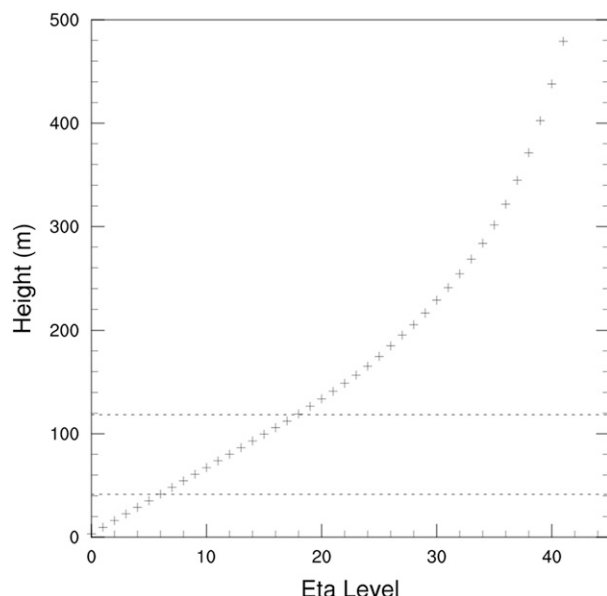


FIG. 1. Eta levels used for this study, as well as their corresponding heights.

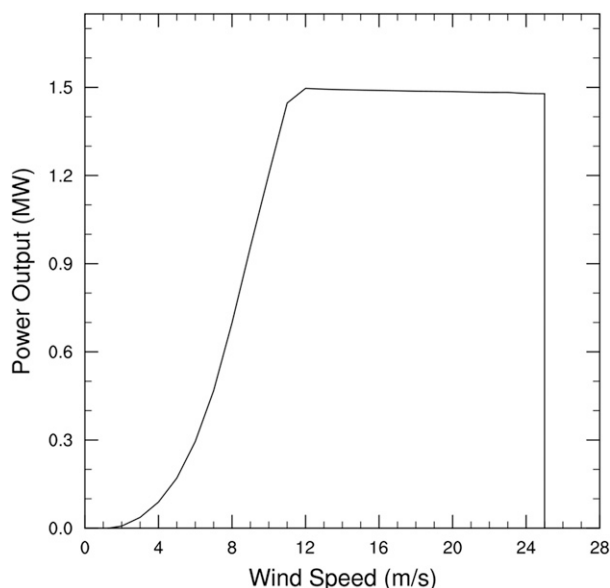


FIG. 2. Power curve for the PSU Generic 1.5 MW Wind Turbine (Schmitz 2011).

surface is flat with a specified roughness length of 0.01 m and a pressure of 1013 hPa. This surface roughness length has been selected to minimize turbulent mixing in the lowest model layer, to make it easier to maintain stratification in the initialized profiles. An f plane with a Coriolis parameter of 10^{-4} s^{-1} is used.

b. Physics

The simulation environment uses only surface layer and planetary boundary layer physics. Both are parameterized using the Mellor–Yamada–Nakanishi–Niino (MYNN) level-2.5 scheme (Mellor and Yamada 1982; Nakanishi and Niino 2009). Under this scheme TKE alone is treated as a prognostic variable, while all other higher-order moments are diagnostically calculated. Modifications to the MYNN scheme’s LES-derived closure constants (Benjamin et al. 2016, their appendix B), which are employed in this study, completely remove the critical Richardson number (Ri) of 1, allowing very small mixing to occur even at very large Ri. Given enough time, wind shear will always mix out. Initializing profiles with $\text{Ri} = 2$ was found to be sufficient to maintain quasi-steady-state, high vertical wind shears for the time lengths used in test simulations. The MYNN uses a dynamic turbulence length scale that varies according to atmospheric static stability and TKE. TKE advection has been enabled in the boundary layer. For these simulations, the model is configured such that only the surface momentum flux is calculated in the MYNN surface layer scheme, as the heat and moisture fluxes are turned off. The atmosphere is dry and remains dry in the

absence of these surface fluxes. This simplified configuration is the same one used by F2012 and is employed here so that comparisons between the two studies may be made.

The wind farm is laid out in a 10×10 grid, with one turbine per cell, centered in the fine domain. The coarse grid contains no wind turbines. In contrast to F2012, an open source 1.5-MW wind turbine, based off the GE SLE 1.5 MW, is used for the farm, with a hub height of 80 m and a rotor diameter of 77 m (Schmitz 2011). The cut-in speed is 3 m s^{-1} and the cut-out speed is 25 m s^{-1} (Fig. 2). Winds blowing outside of this velocity range will not rotate the blades or generate power. Power output reaches its maximum at wind speeds of 12 m s^{-1} , above which it remains approximately constant before eventually cutting out.

c. Dynamics

The WRF Model uses a third-order Runge–Kutta time integration scheme. The model is configured to reduce the impacts of gravity waves on the simulation results by using an implicit gravity wave dampening layer in the uppermost 5 km of the model domain, in accordance with Klemp et al. (2008), to prevent gravity wave reflection off the model top.

Simple horizontal diffusion is employed, with second-order diffusion gradients calculated along coordinate surfaces, which do not use full metric terms. The horizontal eddy diffusion is calculated using the Smagorinsky first-order closure approach with a coefficient of 0.25. Additionally, sixth-order horizontal diffusion has been

activated on model levels, which prevents upgradient diffusion and reduces $2\text{-}\Delta x$ wavelength-characterized noise (Knievel et al. 2007).

d. Initial conditions

The RWFP is tested in a series of different idealized atmospheric environments specified by a user-supplied sounding. This sounding contains initial values of domain potential temperature, pressure, inverse air density, and winds, which are calculated using the geostrophic wind balance and interpolated to eta levels.

To spin up the model, the entire setup—that is, both domains in their full 3D configurations—is run without the wind farm present for a period on the order of days until a steady state is reached. Steady state is defined by the reduction of the amplitude of inertial oscillations in the winds throughout the domain to less than $\sim 2\%$ of the basic-state wind speeds. For each subsequent test simulation, the model is restarted from this state, with different WFP configurations. This method significantly reduces the amount of computation resources needed, as the simulation environment does not need to be spun up for each test run.

4. Simulation overviews

Because of the large number of simulations evaluated in this study, a set of acronyms has been defined to reference each one from this point forward. The cases, descriptions, and acronyms can be found in Table 1.

a. Neutral profiles (cases NF, NR, NV, NB)

A base case simulation is executed for verification purposes. It uses the same initial and forcing conditions as F2012. This environment has constant geostrophic winds blowing at 10 m s^{-1} from the model bottom to the model top. The atmosphere is neutrally stratified up to 1000 m, above which a lapse rate is initialized at a constant, stable 3 K km^{-1} . The surface temperature is 285 K. After spinup, the atmosphere equilibrates into a neutral thermal profile with slight variation in wind speed and direction across the rotor plane (Figs. 3a,b). This simulation is evaluated using both the WFP (NF) and the RWFP (NR, NV, NB). Very little sensitivity to the WFP modifications is anticipated in neutral conditions, so we expect relatively consistent results with F2012.

b. Stable profiles with linear wind shear (cases SF, SR, SV, SB)

To assess the role of shear, a series of simulations defined by linear wind shear across the rotor plane is evaluated. The thermodynamics for these cases are

all strongly stable below 120 m, with a lapse rate of 0.1 K m^{-1} from the ground to 40 m and a potential temperature profile defined by a Richardson number of 2 between 40 and 120 m. Above 120 m, the atmosphere has a stable 3 K km^{-1} lapse rate, as in the previous cases. The winds are calm at 0 m s^{-1} up to 40 m, then increase to 6, 8, or 10 m s^{-1} (cases ending with 06, 08, and 10, respectively) between 40 and 120 m, above which they remain constant at these values. The winds are initialized to blow zonally only. The robust near-surface inversion is necessary to maintain wind shear in the model; without substantial stability, the winds would mix out to develop a relatively uniform profile throughout the boundary layer. These cases are only spun up for 5 days, which is sufficient to limit noise from gravity waves propagating within the model domain.

c. Nonlinear wind shear (cases MF, MR, MV, MB)

To further examine the effects of the REWS and veer awareness, we evaluate a stable case with high wind shear related to cold pool mix-out. The initial and forcing conditions are based on observational data obtained during WFIP2, a field campaign focused on improving model forecasts of low-level winds over complex terrain (Shaw et al. 2018, manuscript submitted to *Bull. Amer. Meteor. Soc.*). The study relies on observations taken by a dense multiscale network of lidars, sodars, and wind profiling radars located in the U.S. Pacific Northwest's Columbia River basin, where numerous wind farms are located (Wilczak et al. 2018, manuscript submitted to *Bull. Amer. Meteor. Soc.*). Data for the project were collected between 1 October 2015 and 31 March 2017 and have captured weather conditions related to cold pools in mountain valleys.

We selected a cold pool mix-out event from 13 January 2016. The profile has been adjusted slightly because the most prominent wind shear is visible across a larger and higher plane than would affect most turbines currently in operation, including the one we have used. Future wind installations will be influenced by a mix-out event like this one as turbines grow in size (Blaabjerg 2013; Wiser et al. 2016).

To represent this mix-out event at discrete stages in an idealized framework, a series of three simplified, staggered profiles are simulated. The cold pool is depicted by a layer of relatively calm, easterly winds. The top of the cold pool varies by simulation, from 80 to 60 m, which represents the sinking of upper-level winds during the mix-out. Above the cold pool are southwesterly winds increasing in speed to 8 m s^{-1} at the top of the rotor plane. To prevent rapid near-surface turbulence generation and homogenization of the winds, a strongly stable Richardson number of 2 is maintained for the thermal profile from 0 to 120 m. Above 120 m, winds are

TABLE 1. Overview of idealized simulations.

Acronym for run	Stability	Wind speed (WS) change across vertical region of interest	Delta T across rotor disk	RWFP or WFP?	Initial veer across rotor disk	
NBASE	Neutral	Constant WS at 10 m s^{-1}	Constant T at 280 K	No WFP	No veer	
NF	Neutral	Constant WS at 10 m s^{-1}	Constant T at 280 K	WFP	No veer	
NR	Neutral	Constant WS at 10 m s^{-1}	Constant T at 280 K	RWFP, REWS only	No veer	
NV	Neutral	Constant WS at 10 m s^{-1}	Constant T at 280 K	RWFP, veer only	No veer	
NB	Neutral	Constant WS at 10 m s^{-1}	Constant T at 280 K	RWFP, REWS and veer	No veer	
SF_06	Stable linear	a. $0\text{--}6\text{ m s}^{-1}$	a. 284–311 K	WFP	No veer	
SF_08		b. $0\text{--}8\text{ m s}^{-1}$	b. 284–334 K			
SF_10		c. $0\text{--}10\text{ m s}^{-1}$	c. 284–365 K			
SR_06	Stable linear	a. $0\text{--}6\text{ m s}^{-1}$	a. 284–311 K	RWFP, REWS only	No veer	
SR_08		b. $0\text{--}8\text{ m s}^{-1}$	b. 284–334 K			
SR_10		c. $0\text{--}10\text{ m s}^{-1}$	c. 284–365 K			
SV_06	Stable linear	a. $0\text{--}6\text{ m s}^{-1}$	a. 284–311 K	RWFP, veer only	No veer	
SV_08		b. $0\text{--}8\text{ m s}^{-1}$	b. 284–334 K			
SV_10		c. $0\text{--}10\text{ m s}^{-1}$	c. 284–365 K			
SB_06	Stable linear	a. $0\text{--}6\text{ m s}^{-1}$	a. 284–311 K	RWFP, REWS and veer	No veer	
SB_08		b. $0\text{--}8\text{ m s}^{-1}$	b. 284–334 K			
SB_10		c. $0\text{--}10\text{ m s}^{-1}$	c. 284–365 K			
MF_60	Stable mix-out	Constant 2 m s^{-1} to	a. 284–469 K	WFP	135° at	
MF_70		a. 60 m	b. 284–487 K		a. 60 m	
MF_80		b. 70 m	c. 284–515 K		b. 70 m	
		c. 80 m			c. 80 m	
		All increase to 8 m s^{-1} at 120 m				
MR_60	Stable mix-out	Constant 2 m s^{-1} to	a. 284–469 K	RWFP, REWS only	135° at	
MR_70		a. 60 m	b. 284–487 K		a. 60 m	
MR_80		b. 70 m	c. 284–515 K		b. 70 m	
		c. 80 m			c. 80 m	
		All increase to 8 m s^{-1} at 120 m				
MV_60	Stable mix-out	Constant 2 m s^{-1} to	a. 284–469 K	RWFP, veer only	135° at	
MV_70		a. 60 m	b. 284–487 K		a. 60 m	
MV_80		b. 70 m	c. 284–515 K		b. 70 m	
		c. 80 m			c. 80 m	
		All increase to 8 m s^{-1} at 120 m				
MB_60	Stable mix-out	Constant 2 m s^{-1} to	a. 284–469 K	RWFP, REWS and veer	135° at	
MB_70		a. 60 m	b. 284–487 K		a. 60 m	
MB_80		b. 70 m	c. 284–515 K		b. 70 m	
		c. 80 m			c. 80 m	
		All increase to 8 m s^{-1} at 120 m				

held constant (both in direction and intensity), and the lapse rate is stable at 3 K km^{-1} up to the model top.

5. Results

a. Comparison with F2012

An initial comparison with the F2012 results has been conducted to verify proper setup of the simulation environment and to assess how WRF updates in more recent releases will impact WFP results. Some differences emerge between the two studies, which may be explained by the comparisons found in Table 2. Overall the findings validate the domain and wind farm parameterization setup.

A wake evolves downwind of the wind farm, with maximum wind speed deficits of 1.82 m s^{-1} —stronger

than the F2012 maximum of 1.5 m s^{-1} . The wake has an e -folding distance through the center of the farm, along the wind direction vector, of 27.3 km (Fig. 4a). About 2 km upwind of the farm, an induction zone wind speed deficit begins to form, beginning at -0.04 m s^{-1} and reaching -0.76 m s^{-1} at the farm's leading edge. F2012 saw deficits peaking at 0.1 m s^{-1} . A small acceleration flanks the wake, with a slightly larger magnitude (0.2 m s^{-1}) on the north side than was seen by Fitch, whose maximum acceleration was 0.1 m s^{-1} . Similar to F2012, the deceleration of winds ahead of the wind farm extends vertically, perturbing the top of the boundary layer (Fig. 4c). Wind speed deficits peak at hub height, at the rear edge of the farm.

The TKE impacts deviate from F2012 (Fig. 4b). Unlike F2012, in this study TKE is enhanced within the

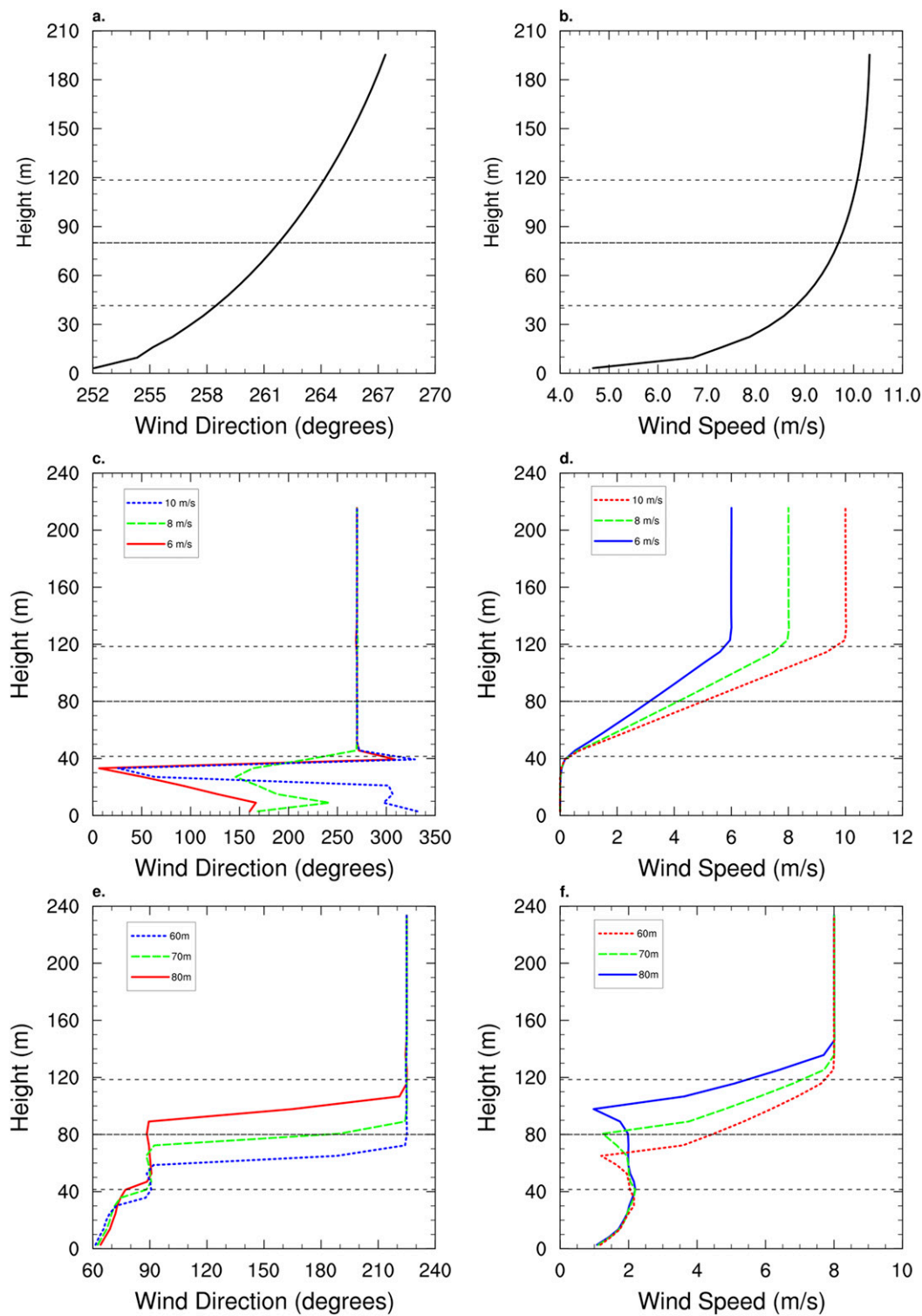


FIG. 3. Postspinup wind direction and wind speeds for the (a),(b) neutral; (c),(d) stable; and (e),(f) mix-out simulations.

TABLE 2. Comparison between F2012 and the present study.

	F2012	Present study
Turbine	Repower 5M	Open-source GE SLE 1.5MW
Temporal averaging	6 h	12 h
Skin surface temperature	285 K	280 K
Surface PRESSURE	1000 hPa	1013 hPa
Inversion location	Unknown	200 m
Eta levels	Unknown	Fig. 1
WRF version	3.3	3.8.1
WFP version	2011	2015
Nesting configuration	Two-way	One-way

farm area and advected downwind of the turbines. The increase in TKE is much lower than what was seen in F2012, with a maximum value of $0.04 \text{ m}^2 \text{ s}^{-2}$ at hub height. The maximum increase in TKE across the entire 3D simulation area is $0.16 \text{ m}^2 \text{ s}^{-2}$ and is seen above the farm and downwind of the northeast corner (Fig. 4d). A reduction in TKE occurs below hub height, with the strongest decrease of $-0.04 \text{ m}^2 \text{ s}^{-2}$ occurring at about 35 m above ground. Overall, the TKE impact of the WFP is much weaker in this simulation than in F2012. This difference may be attributed to developments to the MYNN PBL scheme between WRF 3.3 and 3.8 as well as from different turbine types used in this study and F2012.

The power output of the farm is greatest in the front line of turbines. Figure 5a displays the fractional power output of each cell, defined as the time-averaged power output of the cell divided by the maximum power output of any cell. The lowest power output is found in the northeast corner of the array, at location (10, 10), deviating slightly from F2012, which found that the rear-line turbine directly downwind of the highest-production turbine saw the greatest loss in power output. The south-side turbines located near the southeastern corner of the farm, at (8:10, 1), have a greater power output than those located in the rows farther north. These turbines are directly exposed to the southerly wind component but are still partially shielded from the turbines to the west. Overall, these results are very similar to those found in F2012.

*b. New physics options in F2012 setup
(cases NBASE, NF, NR, NV, NB)*

Very little variation emerges between the neutral case results using the WFP and the RWFP. Simulations have been conducted with each of the following enabled: veer-awareness (NV), the rotor-equivalent wind speed (NR), and both options (NB). In general, the NR case sees the largest differences in TKE, wind speed, and power output, but these differences remain on the

order of less than one percent. Although the differences between RWFP cases and the WFP case are negligible, distinct spatial patterns between them do exist. These patterns may grow in magnitude with larger turbine arrays and faster wind speeds.

The wake strength is very slightly increased with NB and NR when compared with the NF case, with negligible change between NV and NF. The e -folding distance in all three RWFP cases remains the same as in the NF case. The largest difference in the magnitude of the wake at hub height occurs in the NR case, where the maximum deficit is 0.5%, stronger (Fig. 6a). These differences in wake intensity are the greatest near the rear of the farm and rapidly erode farther downwind.

TKE for all three test cases deviates only slightly from the NF results. In general, TKE is increased with the new physics options. The maximum TKE at hub height increases by roughly 2% for the NR and NB cases. TKE increases by only 1% for the NV case. These differences are concentrated near the downwind side of the wind farm area (Fig. 6b).

Overall power is increased for all three test cases, on the order of 1.6% (not nominal) or less. The NR case sees the greatest increase throughout the farm, at 1.4 MW total. Although production from the highest output turbines decreases (−9% for NR), output from the lowest production turbines goes up by more (26.5% for NR), resulting in a net overall increase in power output (Fig. 5b). The NB simulation is dominated by the REWS implementation, so its power values are comparable to those in the NR case. The NV simulation deviates only slightly from the NF case.

These small differences between the test cases and the NF simulation may be attributed to slight nonlinearities in the wind shear profiles intersecting the rotor layer (Figs. 3a,b), which affect the rotor-equivalent wind speed and consequently influence the way turbines interact with the atmosphere in these simulations. This effect validates our hypothesis that the modifications will have a small impact in neutral environments. We expect that an increased vertical wind shear would have a greater effect on the model results.

c. Comparing stable cases, constant wind shear with new physics (cases SF, SR, SV, SB)

As with the neutral case, few differences emerge between the WFP and the RWFP in the high wind speed-shear cases. Although vertical wind shear is strong in these simulations (Fig. 3c), the profile is linear and there is no veer across the rotor swept plane (Fig. 3d). This results in the REWS and hub-height wind speeds being very similar for all cases. Therefore, the discrepancies in wakening, TKE development, and power generation once

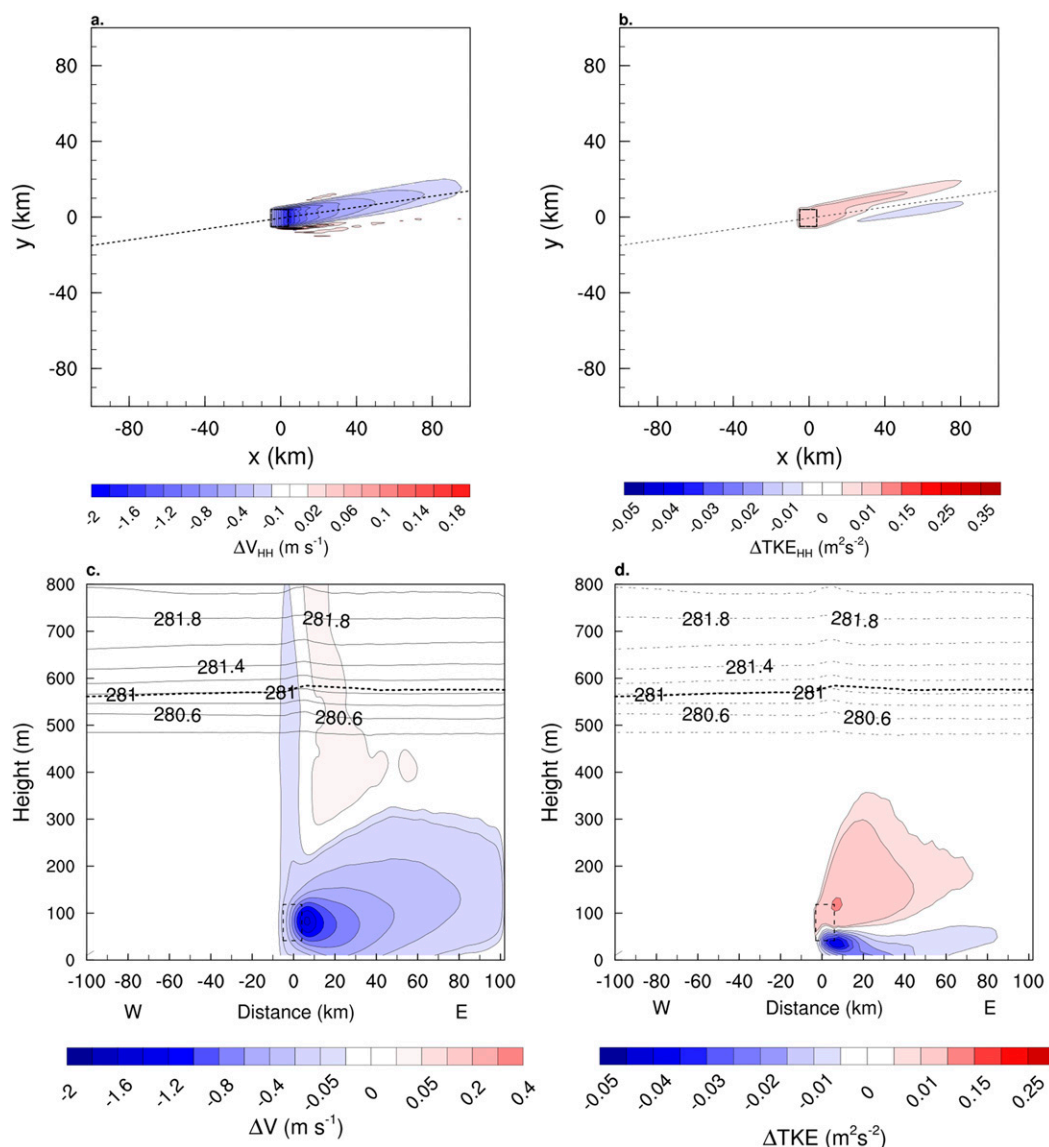


FIG. 4. Horizontal cross section of simulation domain taken at hub height showing the (a) wake and (b) TKE generation. The black dashed outline indicates the wind farm. Vertical cross section taken through the center of the wind farm, along the wind direction vector, showing the (c) wake and (d) TKE generation. The black dashed outline indicates the wind farm, the gray lines show potential temperature, and the thick black dashed line is the top of the boundary layer.

are again nominal, and no meaningful difference emerges between the SV and SF cases.

The SR_06 simulation sees the largest deviation from the SF cases in all three evaluated output variables (wake strength, TKE generation, and power production). At the wake's deepest point, it is enhanced by 0.5%, and at its shallowest point it declines by 1.3%. Similarly, TKE is increased by 7.7% at its peak, and reduced by 5% at its minimum. Since wind speeds are already low in these simulations, these changes in wakening and TKE are negligible. Overall power output is increased by 8.5%,

or 165 kW, which may also be considered insignificant (not shown).

d. Comparing stable cases, nonlinear wind shear with new physics (cases MF, MR, MV, MB)

Unlike the previous two cases, the cold pool mix-out simulations present more significant differences between RWFP and WFP results. The wind speed and wind direction profiles after spinup (Figs. 3e,f) are highly nonlinear. This “staggering” of the two layers impacts the weighted averaging of the RWFP so that

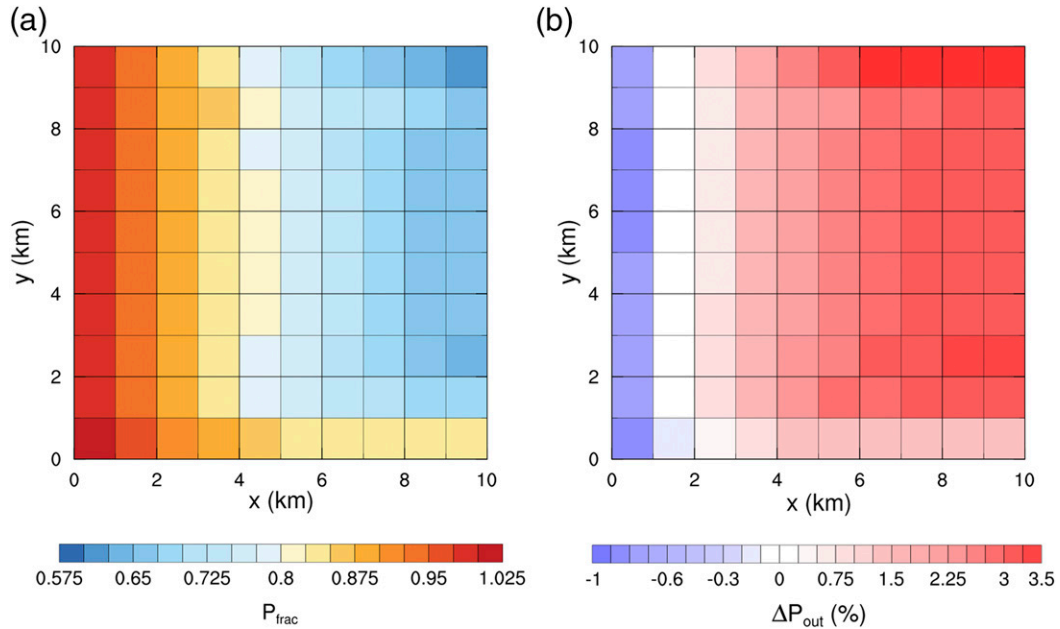


FIG. 5. (a) Fractional power output in each grid cell of the wind farm, defined as the temporal average of power output in the grid cell divided by the maximum power output of any grid cell over the simulation period. (b) Percent difference in power output between the NF and NR simulations.

the REWS deviates significantly from hub-height wind speed. Additionally, this nonlinearity can dictate whether the turbines turn on (MF_70, MV_70) or remain inactive (MR_70, MR_80).

The wake structures strengthen as the inversion moves lower in the atmosphere, analogous to a cold pool being

mixed out. When the inversion is set at 80 m, the turbines do not activate, as both hub height and REWS wind speeds are below the cut-in speed of 3 m s^{-1} . At 70 m, wind speeds are high enough to turn on the turbines for the MF_70 and MV_70 cases. However, the turbines in MR_70 and MB_70 remain off. The influence of the

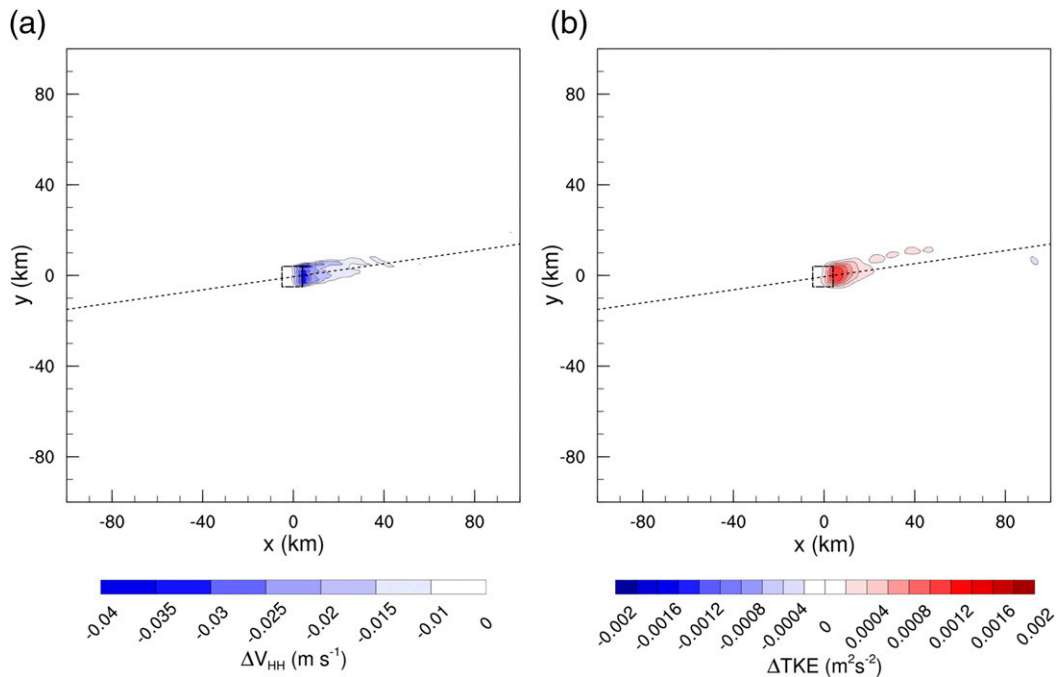


FIG. 6. Difference between the (a) waking and (b) TKE generation in the NR and NF simulations. Negative values in (a) indicate a stronger wake, and positive values in (b) indicate greater TKE.

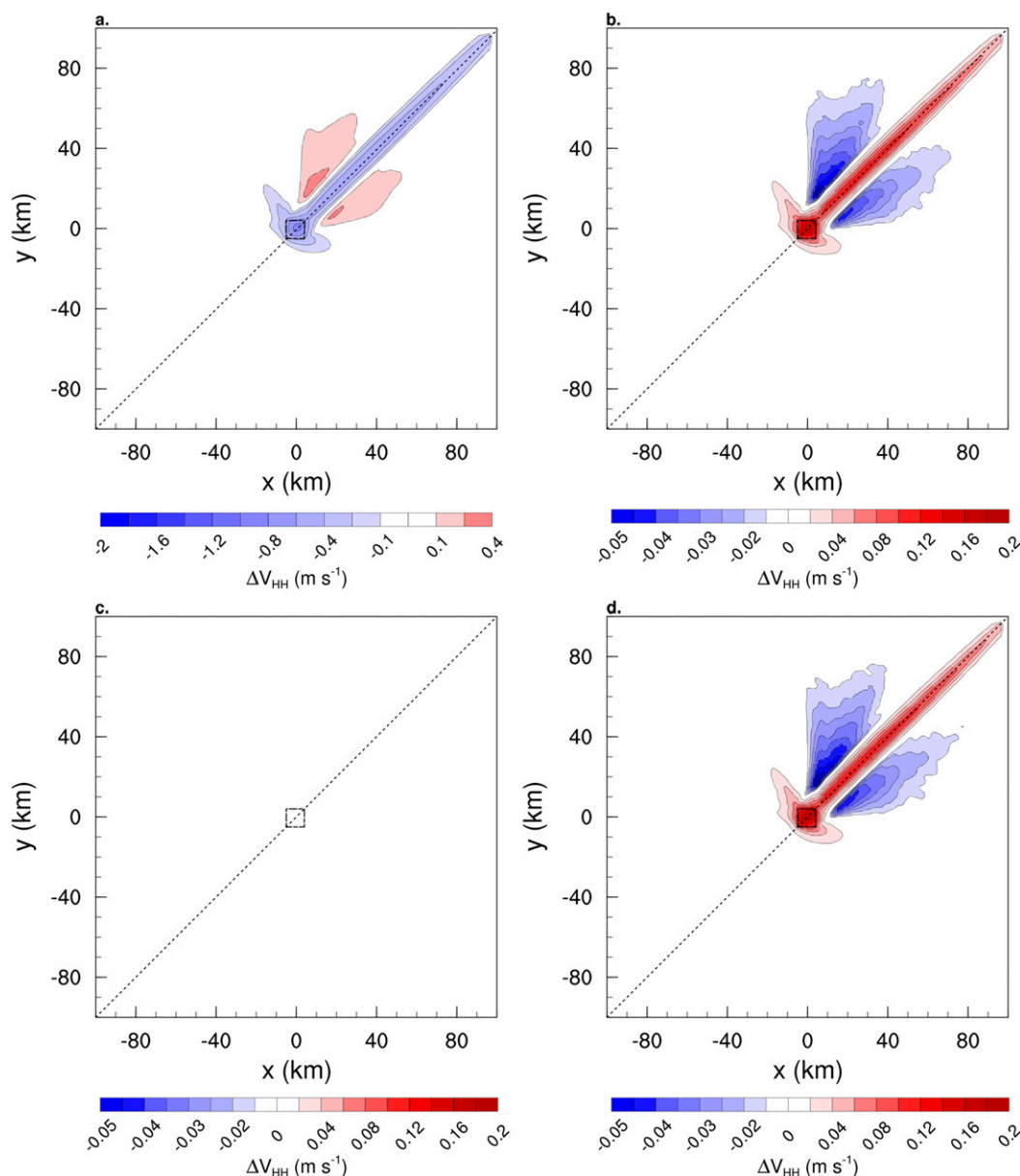


FIG. 7. (a) Waking and acceleration of winds in the MF₆₀ simulation. Differences between the waking in (b) MR₆₀, (c) MV₆₀, (d) MB₆₀, and MF₆₀. Positive values in (b)–(d) indicate a weakening of the wake. Negative values along the flanks indicate a weakening of the acceleration on either side of the wake.

REWS lowers wind speeds seen by the turbines to below-cut-in levels. At 60 m, all turbines are on. The M₆₀ simulations, therefore, highlight how the different WFP physics influence the winds seen by the turbines and the strengths of the wakes they produce (Fig. 7). The REWS tends to reduce the wind speed driving the turbines during cold-pool mix-outs, while veer awareness has a nominal effect. The maximum wake of the MR₆₀ case is weakened by 4.7%. With veer-awareness added to REWS (MB), this reduction in wake strength is slightly larger, 4.9%.

The differences in TKE generation are negligible, with the greatest impacts being seen in the MB cases. The largest change is a 12% reduction in the minimum TKE produced in the MB₆₀ case, as compared with the MF₆₀ case. However, since the TKE is already so low to begin with, this change is trivial.

Power production begins as the inversion drops low enough to raise wind speeds above the cut-in velocity of 3 m s^{-1} . As was seen with the waking differences, the REWS reduces the wind speeds driving the turbines.

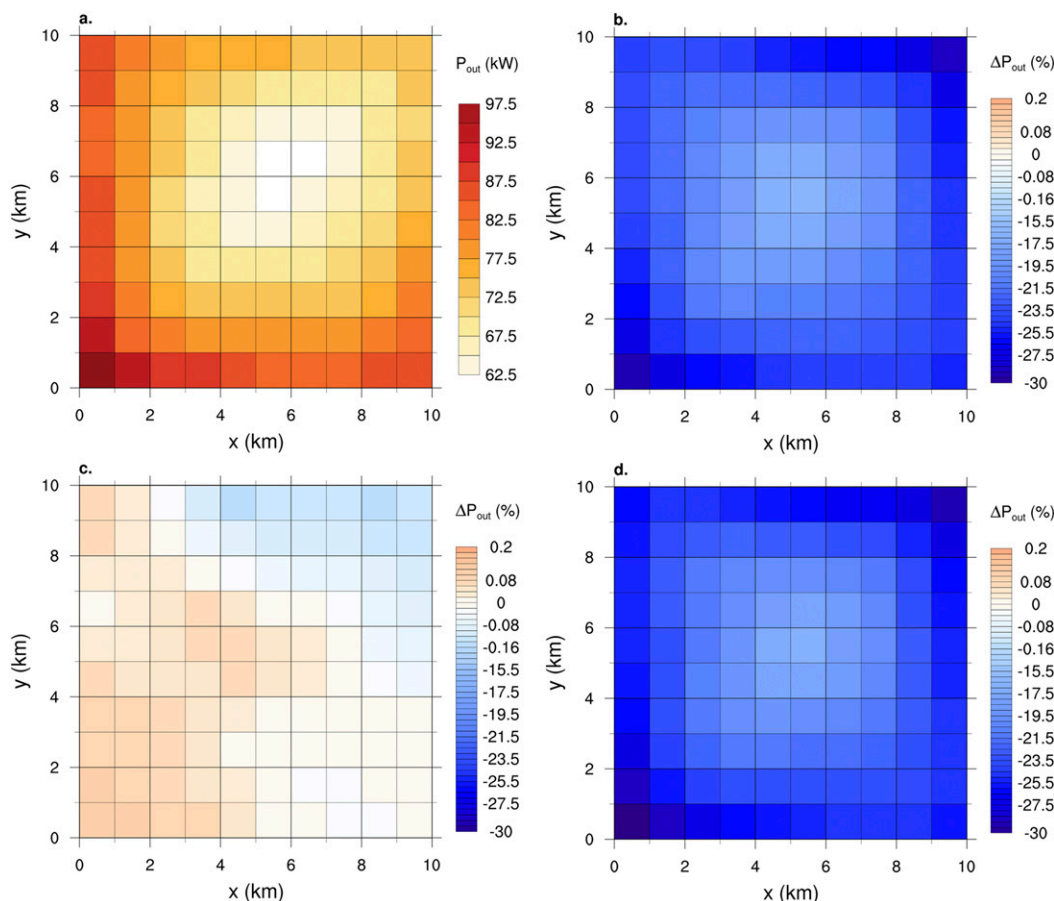


FIG. 8. (a) Power output for the MF_60 simulation (in kW). Percent change in power output between (b) MR_60, (c) MV_60, (d) MB_60, and MF_60.

Therefore, turbines in the MF and MV simulations cut in when the inversion drops to 70 m, but the MR and MB cases do not experience strong enough winds to activate their turbines until the inversion lowers to 60 m (Fig. 8). In these simulations, the smaller REWS, compared with hub-height winds, results in 41.5% less power production for MR_60 and 44% less for MB_60. Veer awareness has a mixed, yet negligible, impact on power production. At lower wind speeds (MV_70), it increases power output by 3.2%; however, as the velocity increases, this impact drops to 0.003% (not shown).

6. Discussion and conclusions

This study compares the WRF 3.8.1 WFP scheme with a revised WFP (RWFP) that includes two new wind-turbine physics options: 1) the use of the rotor-equivalent wind speed (REWS) instead of hub-height wind speed and 2) the consideration of wind veer across the rotor swept plane. Several simulation environments are set up and evaluated. All are run with the idealized

WRF framework. Comparisons are made between results obtained using the WFP and the RWFP. The first set of simulations mirrors the neutral stability setup used by Fitch et al. (2012). The second set of simulations is run in a stable environment with linear wind shear across the rotor layer. The final set of simulations represents a cold pool mix-out—a phenomenon that occurs in the Pacific Northwest's Columbia River basin (Whiteman et al. 2001).

Despite former studies emphasizing the potential impact of the REWS, we find that there are few differences in wake development, TKE generation, and power output between the WFP and RWFP for common neutrally and stably stratified cases. With a neutrally stratified profile, wind shear is low, so the RWFP and the standard WRF WFP scheme return similar results (a 0.5% difference in wake strength). In the stable profile cases, wind shear is mostly linear across the rotor swept plane. The REWS and hub-height wind speeds are therefore similar. The greatest difference in wakening magnitude is 1.3%. Although the physics changes exert some minor influence

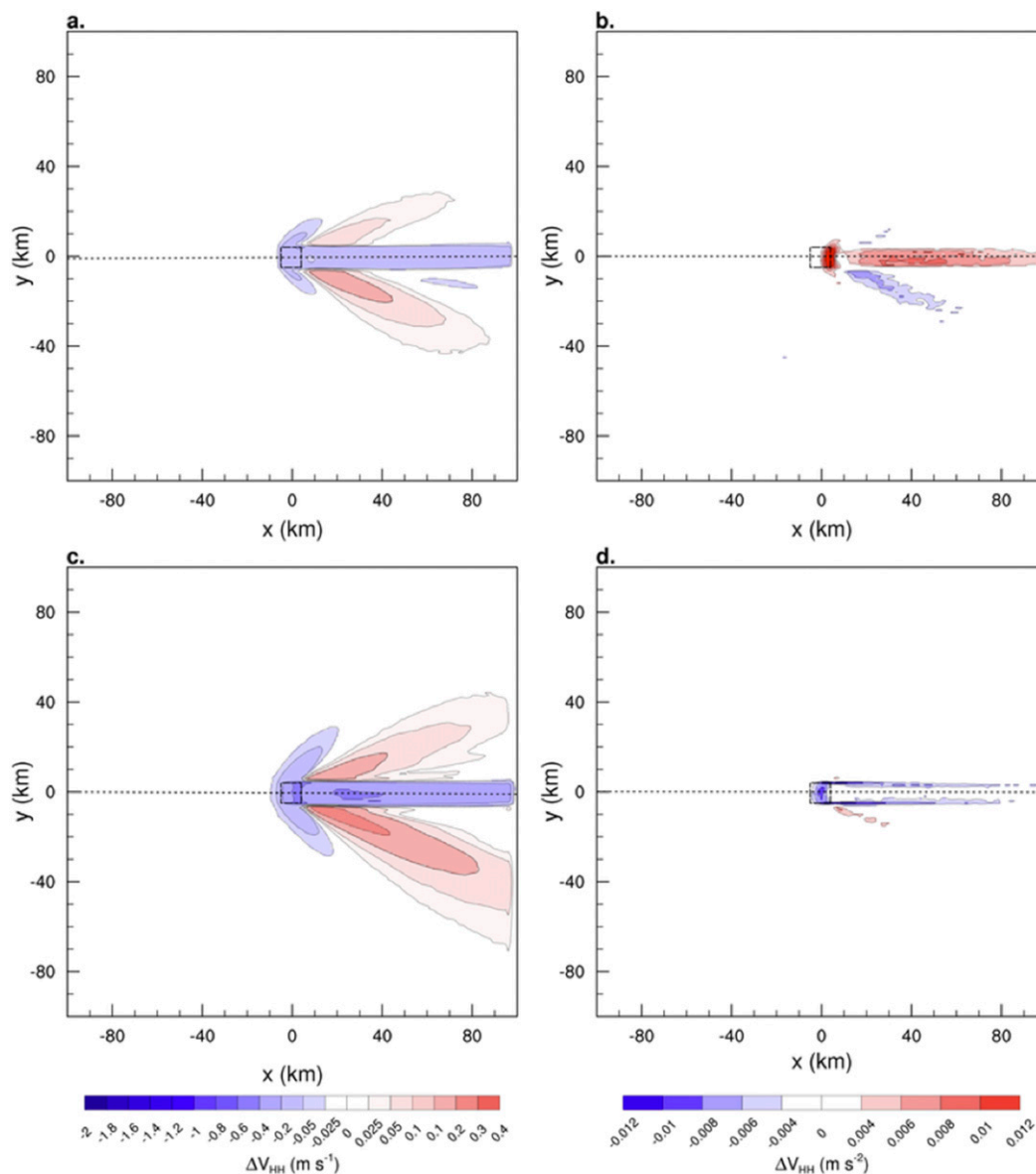


FIG. A1. Hub height wind (80 m) speed differences between the RWFP (REWS only) and the WFP in a stable environment. The plots on the left-hand side depict the wakes seen with the WFP in (a) SR_06 and (c) SR_10. The right-hand side plots show the differences in waking between the REWS RWFP and the WFP in (b) SR_06 and (d) SR_10.

over the results, as indicated by spatial patterns, the magnitude of the resulting differences is small enough to be considered insignificant.

Even though the first two sets of simulations indicated little impact from the RWFP, the RWFP does have significant implications for the case of the cold pool mix-out—an environment with high, nonlinear wind shear and veer. The new physics options can make the difference between the wind turbines cutting in or remaining inactive, and the use of the REWS can appreciably affect waking and power production. To better understand the

implications of our results, we recommend future research that compares RWFP and WFP results with observational data.

Based on our findings, we conclude that for most cases, the RWFP does not affect model performance in a significant manner. The WFP, therefore, is adequate for most wind power forecasting projects. However, for regions where cold pool mix-out events do occur with regularity—such as the Columbia River basin, where over 6 GW of wind energy is installed and where cold pools are commonplace in the cool season

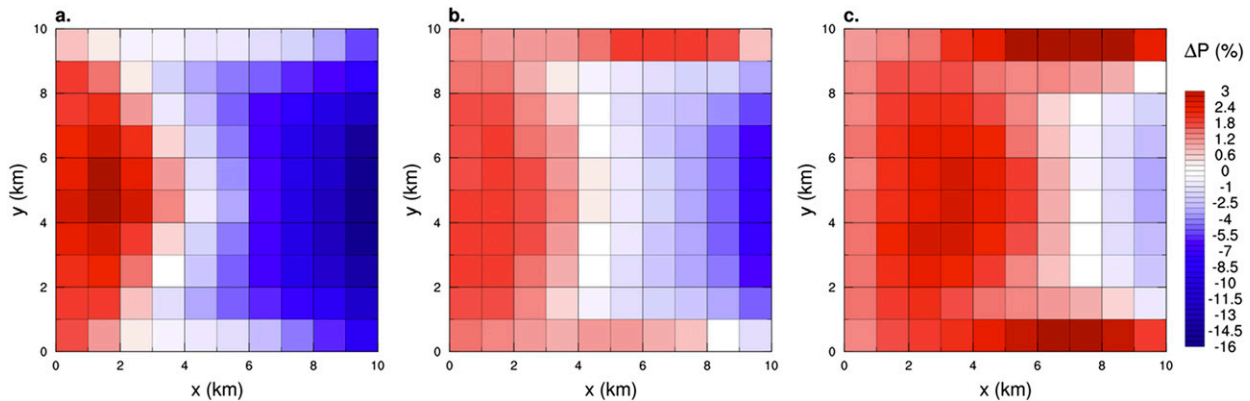


FIG. A2. Percentage differences in average power output between the WFP and the RWFP (REWS only) in a stable environment for (a) SR_06, (b) SR_08, and (c) SR_10.

(Whiteman et al. 2001; Wilczak et al. 2018, manuscript submitted to *Bull. Amer. Meteor. Soc.*)—the RWFP can increase the accuracy of wind forecasts. Mountainous regions tend to see the highest amounts of wind shear, so the RWFP should have the largest impact in these areas (Clack et al. 2016). In particular, the final set of results demonstrate that the RWFP may be especially useful for timing the activation of turbines during wind ramp-up or ramp-down events, which occur on short time scales (typically less than a few hours). Additionally, certain low-level jets (LLJs) in very stable boundary layers, as well as some near-surface inversions, can have wind shear similar to what we have modeled in the mix-out simulations. However, the wind speeds in low-level jets dipping close to the planetary surface are typically weak and the shear, therefore, is weak as well (Bonner 1968; Banta et al. 2002, 2007). We advise that further testing of the RWFP using LLJ observations be conducted to conclusively establish the impact of these events.

Acknowledgments. Stephanie Redfern was supported by a fellowship from NOAA GSD (Award NA17OAR4320101). Julie K. Lundquist was supported by the National Science Foundation (Grant 1413980; project title CNH-Ex: Legal, Economic, and Natural Science Analyses of Wind Plant Impacts and Interactions).

APPENDIX

Influence of TKE Advection on Results

A second set of simulations was run with TKE advection turned off, in order to evaluate the new WFP physics in a modeling environment consistent with that used in the National Oceanic and Atmospheric Administration (NOAA)'s operational Rapid

Refresh forecast system (Benjamin et al. 2016). The lack of TKE advection had some significant impacts on the results.

a. Neutral case

The TKE generation in the neutral stability simulation was stronger than with TKE advection turned off. The TKE increase within the wind farm reaches a maximum of $0.4 \text{ m}^2 \text{ s}^{-2}$ —about 7 times greater than a simulation run without the WFP. It also remains constrained within the farm area, instead of being advected downwind. The TKE spreads directly upward from the farm to the base of the inversion, slightly perturbing the boundary layer, as seen in the LES of Allaerts and Meyers (2018), as well as in F2012. The most prominent difference between these results and those of F2012 is the extension of TKE downwind peaking at around 200 m above ground and rapidly decaying in the horizontal at higher altitudes. This phenomenon may be directly attributed to this lack of TKE advection.

b. Stable, linear wind shear case

Although the magnitude of the impacts from the new WFP physics remains nominal for the linearly stable simulations, without TKE advection enabled some clear spatial patterns emerge—primarily in the wake development and power production. As wind speeds increase across the rotor plane, the RWFP moves from weakening the wake to strengthening it (Fig. A1). The greatest instance of wake weakening occurs in the SR_60 and the SB_60 cases, with a maximum reduction as compared with the WFP wake of 0.018 m s^{-1} . With higher wind speeds, the RWFP wake begins to intensify within the farm and spread around its flanks downstream. This widening and fortification likely emerges due to the lateral entrainment of momentum via horizontal diffusion, which mixes higher

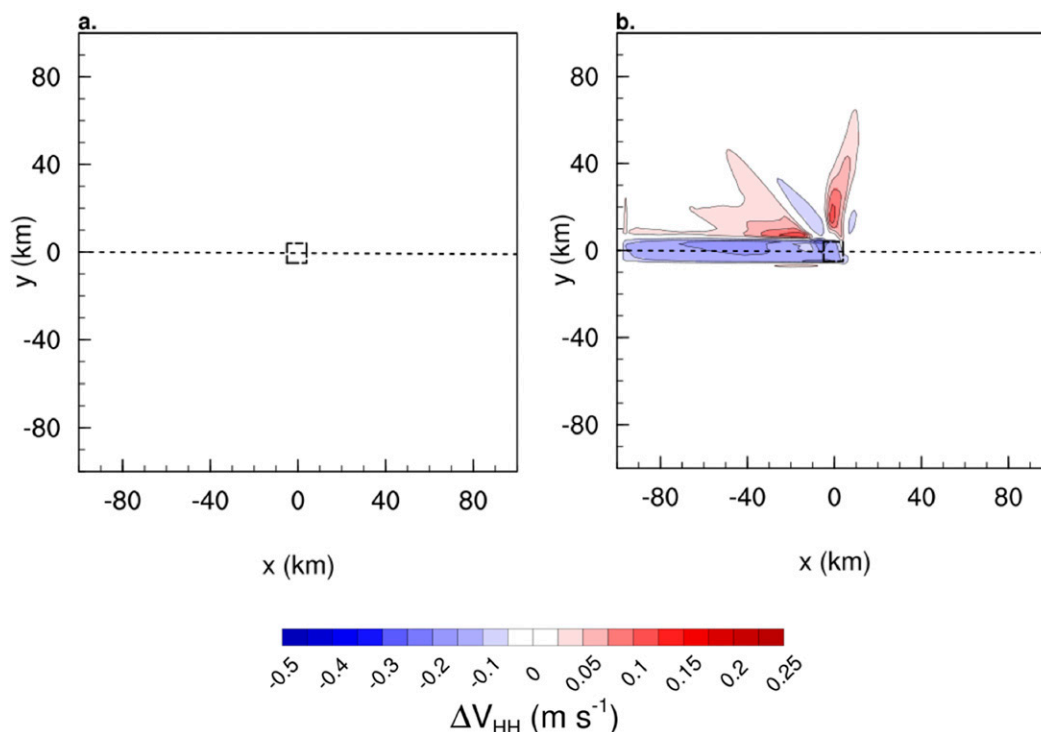


FIG. A3. (a) The left plot depicts the wakes that develop at hub height (80 m) when the WFP is activated for the cold pool mix-out simulation with the inversion level at 80 m (M_80). The wind speed at hub height is below the cut-in speed for the turbines, so they do not produce power. (b) The right plot depicts the difference in waking between the REWS and WFP simulations with the 80 m inversion level. The REWS enables the turbines to see a wind speed above the cut-in velocity, and the turbines produce power and generate wakes.

wind speeds into the farm along its north and south edges. The SR_10 case sees the greatest wake strengthening with a maximum increase of 0.011 m s^{-1} .

Power output varies only slightly between the RWFP and WFP schemes and these variations correspond with the differences in waking (Fig. A2). Front-row turbines using the REWS see an increase in their power output and downstream turbines experience a decrease for all SR and SB cases. The largest difference in total wind farm average power output arises at smaller wind speeds. SB_06 sees a 3.29%, or about 27.6 kW, reduction in average power compared with SF_06. As wind speeds increase, this mean difference becomes positive. Compared with SB_06, SB_10 sees a 1.25% increase in total average power. The greatest increase in maximum power output for a single turbine occurs in SR_10, with a 3.49% increase over SF_10. The largest reduction in minimum power output for a single turbine is seen in SB_06, with a 16.27% decrease.

c. Stable, nonlinear wind shear case

Without TKE advection turned on, the cold pool mix-out simulations highlight two new impacts from

the RWFP physics. First, the REWS and veer-awareness appear to interact in a nonlinear fashion. When both options are enabled, their combined influence has a much greater impact on the wakes and power generated by the turbines than either option alone. Second, unlike with the TKE advection-enabled simulations, the REWS can be stronger than the hub-height wind speed. For wind speeds near the cut-in value, the REWS-only turbines can turn on when they remain off for simulations using the other physics schemes (including REWS and veer-awareness together), as in MR_80 (Fig. A3).

REFERENCES

- Allaerts, D., and J. Meyers, 2018: Gravity waves and wind-farm efficiency in neutral and stable conditions. *Bound.-Layer Meteor.*, **166**, 269–299, <https://doi.org/10.1007/s10546-017-0307-5>.
- Armstrong, A., R. R. Burton, S. E. Lee, S. Mobbs, N. Ostle, V. Smith, S. Waldron, and J. Whitaker, 2016: Ground-level climate at a peatland wind farm in Scotland is affected by wind turbine operation. *Environ. Res. Lett.*, **11**, 044024, <https://iopscience.iop.org/article/10.1088/1748-9326/11/4/044024>.
- AWEA Data Services, 2017: U.S. wind industry fourth quarter 2017 market report. American Wind Energy Association, 17 pp.,

- <https://www.awea.org/resources/publications-and-reports/market-reports/2017-u-s-wind-industry-market-reports>.
- Baidya Roy, S., 2011: Simulating impacts of wind farms on local hydrometeorology. *J. Wind Eng. Ind. Aerodyn.*, **99**, 491–498, <https://doi.org/10.1016/j.jweia.2010.12.013>.
- , and J. J. Traiteur, 2010: Impacts of wind farms on surface air temperatures. *Proc. Natl. Acad. Sci. USA*, **107**, 17 899–17 904, <https://doi.org/10.1073/pnas.1000493107>.
- , S. W. Pacala, and R. L. Walko, 2004: Can large wind farms affect local meteorology? *J. Geophys. Res.*, **109**, D19101, <https://doi.org/10.1029/2004JD004763>.
- Banta, R. M., R. K. Newsom, J. K. Lundquist, Y. L. Pichugina, R. L. Coulter, and L. Mahrt, 2002: Nocturnal low-level jet characteristics over Kansas during CASES-99. *Bound.-Layer Meteor.*, **105**, 221–252, <https://doi.org/10.1023/A:1019992330866>.
- , L. Mahrt, D. Vickers, J. Sun, B. B. Balsley, Y. L. Pichugina, and E. J. Williams, 2007: The very stable boundary layer on nights with weak low-level jets. *J. Atmos. Sci.*, **64**, 3068–3090, <https://doi.org/10.1175/JAS4002.1>.
- Benjamin, S. G., and Coauthors, 2016: A North American Hourly Assimilation and Model Forecast Cycle: The Rapid Refresh. *Mon. Wea. Rev.*, **144**, 1669–1694, <https://doi.org/10.1175/MWR-D-15-0242.1>.
- Blaabjerg, F., 2013: Future on power electronics for wind turbine systems. *IEEE J. Emerging Sel. Top. Power Electron.*, **1**, 139–152, <https://doi.org/10.1109/JESTPE.2013.2275978>.
- Blahak, U., B. Goretzki, and J. Meis, 2010: A simple parameterization of drag forces induced by large wind farms for numerical weather prediction models. *Proc. European Wind Energy Conf. and Exhibition*, PO ID 445, Warsaw, Poland, EWEC, 186–189.
- Bonner, W. D., 1968: Climatology of the low level jet. *Mon. Wea. Rev.*, **96**, 833–850, [https://doi.org/10.1175/1520-0493\(1968\)096<0833:COTLLJ>2.0.CO;2](https://doi.org/10.1175/1520-0493(1968)096<0833:COTLLJ>2.0.CO;2).
- Choukulkar, A., Y. Pichugina, C. T. M. Clack, R. Calhoun, R. Banta, A. Brewer, and M. Hardesty, 2016: A new formulation for rotor equivalent wind speed for wind resource assessment and wind power forecasting. *Wind Energy*, **19**, 1439–1452, <https://doi.org/10.1002/we.1929>.
- Clack, C. T. M., A. Alexander, A. Choukulkar, and A. E. MacDonald, 2016: Demonstrating the effect of vertical and directional shear for resource mapping of wind power. *Wind Energy*, **19**, 1687–1697, <https://doi.org/10.1002/we.1944>.
- Fitch, A. C., 2015: Climate impacts of large-scale wind farms as parameterized in a global climate model. *J. Climate*, **28**, 6160–6180, <https://doi.org/10.1175/JCLI-D-14-00245.1>.
- , 2016: Notes on using the mesoscale wind farm parameterization of Fitch et al. (2012) in WRF. *Wind Energy*, **19**, 1757–1758, <https://doi.org/10.1002/we.1945>.
- , J. B. Olson, J. K. Lundquist, J. Dudhia, A. K. Gupta, J. Michalak, and I. Barstad, 2012: Local and mesoscale impacts of wind farms as parameterized in a mesoscale NWP model. *Mon. Wea. Rev.*, **140**, 3017–3038, <https://doi.org/10.1175/MWR-D-11-00352.1>.
- , J. K. Lundquist, and J. B. Olson, 2013a: Mesoscale influences of wind farms throughout a diurnal cycle. *Mon. Wea. Rev.*, **141**, 2173–2198, <https://doi.org/10.1175/MWR-D-12-00185.1>.
- , J. B. Olson, J. K. Lundquist, J. Dudhia, A. K. Gupta, J. Michalak, I. Barstad, and C. L. Archer, 2013b: Corrigendum. *Mon. Wea. Rev.*, **141**, 1395, <https://doi.org/10.1175/MWR-D-12-00341.1>.
- Global Wind Energy Council, 2018: Global wind statistics 2017. Global Wind Energy Council, Brussels, Belgium, https://gwec.net/wp-content/uploads/vip/GWEC_PRstats2017_EN-003_FINAL.pdf.
- Högström, U., D. N. Asimakopoulos, H. Kambezidis, C. G. Helmig, and A. Smedman, 1988: A field study of the wake behind a 2 MW wind turbine. *Atmos. Environ.*, **22**, 803–820, [https://doi.org/10.1016/0004-6981\(88\)90020-0](https://doi.org/10.1016/0004-6981(88)90020-0).
- Jungo, G. V., Y. T. Wu, and F. Porté-Agel, 2013: Field measurements of wind turbine wakes with lidars. *J. Atmos. Oceanic Technol.*, **30**, 274–287, <https://doi.org/10.1175/JTECH-D-12-00051.1>.
- Jimenez, P. A., J. Navarro, A. M. Palomares, and J. Dudhia, 2015: Mesoscale modeling of offshore wind turbine wakes at the wind farm resolving scale: A composite-based analysis with the Weather Research and Forecasting model over Horns Rev. *Wind Energy*, **18**, 559–566, <https://doi.org/10.1002/we.1708>.
- Klemp, J. B., J. Dudhia, and A. D. Hassiotis, 2008: An upper gravity-wave absorbing layer for NWP applications. *Mon. Wea. Rev.*, **136**, 3987–4004, <https://doi.org/10.1175/2008MWR2596.1>.
- Knievel, J. C., G. H. Bryan, and J. P. Hacker, 2007: Explicit numerical diffusion in the WRF Model. *Mon. Wea. Rev.*, **135**, 3808–3824, <https://doi.org/10.1175/2007MWR2100.1>.
- Lee, J. C. Y., and J. K. Lundquist, 2017a: Observing and simulating turbine wakes during the evening transition. *Bound.-Layer Meteor.*, **164**, 449–474, <https://doi.org/10.1007/s10546-017-0257-y>.
- , and —, 2017b: Evaluation of the wind farm parameterization in the Weather Research and Forecasting model (version 3.8.1) with meteorological and turbine power data. *Geosci. Model Dev.*, **10**, 4229–4244, <https://doi.org/10.5194/gmd-10-4229-2017>.
- Lissaman, P. B. S., 1979: Energy effectiveness of arbitrary arrays of wind turbines. *J. Energy*, **3**, 323–328, <https://doi.org/10.2514/3.62441>.
- Mellor, G. L., and T. Yamada, 1982: Development of a turbulence closure model for geophysical fluid problems. *Rev. Geophys. Space Phys.*, **20**, 851–875, <https://doi.org/10.1029/RG020i004p00851>.
- Nakanishi, M., and H. Niino, 2009: Development of an improved turbulence closure model for the atmospheric boundary layer. *J. Meteor. Soc. Japan*, **87**, 895–912, <https://doi.org/10.2151/jmsj.87.895>.
- Powers, J. G., and Coauthors, 2017: The Weather Research and Forecasting Model: Overview, system efforts, and future directions. *Bull. Amer. Meteor. Soc.*, **98**, 1717–1737, <https://doi.org/10.1175/BAMS-D-15-00308.1>.
- Rajewski, D. A., and Coauthors, 2013: Crop Wind Energy Experiment (CWEX): Observations of surface-layer, boundary layer, and mesoscale interactions with a wind farm. *Bull. Amer. Meteor. Soc.*, **94**, 655–672, <https://doi.org/10.1175/BAMS-D-11-00240.1>.
- , E. S. Takle, J. H. Prueger, and R. K. Doorenbos, 2016: Toward understanding the physical link between turbines and microclimate impacts from in situ measurements in a large wind farm. *J. Geophys. Res. Atmos.*, **121**, 13 392–13 414, <https://doi.org/10.1002/2016JD025297>.
- Schmitz, S., 2011: XTurb-PSU: A wind turbine design and analysis tool, version 1.1. The Pennsylvania State University, accessed 26 June 2016, http://www.aero.psu.edu/Faculty_Staff/schmitz/XTurb/XTurb.html.
- Skamarock, W. C., and Coauthors, 2008: A description of the Advanced Research WRF version 3. NCAR Tech. Note NCAR/TN-475+STR, 113 pp., <https://doi.org/10.5065/D68S4MVH>.
- Smith, C. M., R. J. Barthelmie, and S. C. Pryor, 2013: In situ observations of the influence of a large onshore wind farm on near-surface temperature, turbulence intensity and wind speed profiles. *Environ. Res. Lett.*, **8**, 034006, <https://doi.org/10.1088/1748-9326/8/3/034006>.

- U.S. Energy Information Administration, 2018: What is U.S. electricity generation by energy source? Accessed 27 February 2019, <https://www.eia.gov/tools/faqs/faq.php?id=427&t=3>.
- Vanderwende, B. J., B. Kosović, J. K. Lundquist, and J. D. Mirocha, 2016: Simulating effects of a wind-turbine array using LES and RANS. *J. Adv. Model. Earth Syst.*, **8**, 1376–1390, <https://doi.org/10.1002/2016MS000652>.
- Vautard, R., F. Thais, I. Tobin, F. M. Bréon, J. G. D. De Lavergne, A. Colette, P. Yiou, and P. M. Ruti, 2014: Regional climate model simulations indicate limited climatic impacts by operational and planned European wind farms. *Nat. Commun.*, **5**, 1–9, <https://doi.org/10.1038/ncomms4196>.
- Volker, P. J. H., J. Badger, A. N. Hahmann, and S. Ott, 2015: The explicit wake parametrisation V1.0: A wind farm parametrisation in the mesoscale model WRF. *Geosci. Model Dev.*, **8**, 3715–3731, <https://doi.org/10.5194/gmd-8-3715-2015>.
- Wagner, R., I. Antoniou, S. M. Pedersen, M. S. Courtney, and H. E. Jorgensen, 2009: The influence of the wind speed profile on wind turbine performance measurements. *Wind Energy*, **12**, 348–362, <https://doi.org/10.1002/we.297>.
- Wang, C., and R. G. Prinn, 2010: Potential climatic impacts and reliability of very large-scale wind farms. *Atmos. Chem. Phys.*, **10**, 2053–2061, <https://doi.org/10.5194/acp-10-2053-2010>.
- Whiteman, C. D., S. Zhong, W. J. Shaw, J. M. Hubbe, X. Bian, and J. Mittelstadt, 2001: Cold pools in the Columbia Basin. *Wea. Forecasting*, **16**, 432–447, [https://doi.org/10.1175/1520-0434\(2001\)016<0432:CPITCB>2.0.CO;2](https://doi.org/10.1175/1520-0434(2001)016<0432:CPITCB>2.0.CO;2).
- Williams, E., E. Hittinger, R. Carvalho, and R. Williams, 2017: Wind power costs expected to decrease due to technological progress. *Energy Policy*, **106**, 427–435, <https://doi.org/10.1016/j.enpol.2017.03.032>.
- Wiser, R., M. Hand, J. Seel, and B. Paulos, 2016: Reducing wind energy costs through increased turbine size: Is the sky the limit? Berkeley Lab, 7 pp., https://emp.lbl.gov/sites/all/files/scaling_turbines.pdf.
- Xia, G., M. C. Cervarich, S. B. Roy, L. Zhou, J. R. Minder, P. A. Jimenez, and J. M. Freedman, 2017: Simulating impacts of real-world wind farms on land surface temperature using the WRF Model: Validation with observations. *Mon. Wea. Rev.*, **145**, 4813–4836, <https://doi.org/10.1175/MWR-D-16-0401.1>.
- Zhou, L., Y. Tian, S. B. Roy, C. Thorncroft, and L. F. Bosart, 2012: Impacts of wind farms on land surface temperature. *Nat. Climate Change*, **2**, 539–543, <https://doi.org/10.1038/nclimate1505>.